Modeling of an electrically tunable quantum dot photodetector for terahertz detection

Wei Wu[a], Dibyendu Dey, Omer G. Memis, and Hooman Mohseni[b]

Department of EECS, Northwestern University, 2145 Sheridan Rd, Evanston, IL 60208, USA

ABSTRACT

The terahertz region (1-10 THz) has potential applications in many areas, such as chemical sensing, medical imaging and free-space optical communications. With the demonstration of terahertz sources, it is quite necessary to develop the detection technology in terahertz. Here we propose an electrically tunable quantum dot infrared photodetector to detect the terahertz region. The proposed detector applies a lateral electrical confinement on the quantum wells and forms a quantum disk in the quantum well area. The two-dimensional quantum confinement of quantum disk combining the vertical confinement from the quantum barrier forms a quantum dot structure. Using the energy states and intersublevel energy spacing in the quantum dot, the detector can be used to detect the terahertz region. Changing the lateral electrical confinement, the intersublevel energy spacing can also be tuned and in hence different wavelengths can be detected. Our modeling and simulation results show the tunability of peak detection wavelength of the photodetector from ~3.3 to ~6.0 THz with a gate voltage applied on the detector from -2 to -5 V. The peak absorption coefficients of the detection are shown in the range of 10^3 cm^{-1}. Compared with current quantum dot photodetectors produced by self-assembled growth method the detector proposed here is easier to be tuned and the effective sizes have a much higher uniformity, because of using electrical confinement.

Keywords: photodetector, quantum dots, terahertz, electrical confinement, and tunability

1. Introduction

The terahertz region in the electromagnetic spectrum is loosely defined as the electromagnetic wave with frequency in the range between 1 and 10 Thz (10^{12} Hz)[1]. Because terahertz radiation is non-ionizing radiation and can penetrate a wide variety of non-conducting materials[2], it can be potentially applied into many areas, such as medical imaging, security screening, free-space communication, and chemical molecule sensing[3, 4, 5, 6]. For example, in medical imaging area since terahertz radiation is non-ionizing it has the advantage of being expected not to damage tissues and DNA. In the area of terahertz communications between satellite/aircraft and satellite/aircraft in the high altitude, it has the advantage of effectively avoiding the information being eavesdropped on from ground receivers because of the heavy absorption of water vapor from high altitude to ground. To realize these applications in terahertz region, both reliable and convenient terahertz sources and detectors are required. With recent demonstrations and development of terahertz sources[7, 8, 9], it is quite necessary to develop suitable terahertz detectors. Current terahertz detection mainly uses the methods of frequency conversion or heat production. The available marketable terahertz detectors include Schottky diode mixers[10], photoconductive antennas[11], and silicon bolometers[12] etc. However, these detectors either need sophisticated instrumentation, or are intrinsically slow and need a very low temperature operation. Recently, terahertz detectors utilizing intersubband transitions in semiconductor quantum structures such as quantum well infrared photodetectors (QWIPs)[13] have been developed and promised to have a very fast time response because of the intersubband transition nature. Similar to QWIPs, QDIPs for terahertz region using inter-level transitions have also been

---

[a] wwu@u.northwestern.edu, [b] hmohseni@northwestern.edu, http://bisol.northwestern.edu

demonstrated[14]. Compared with QWIPs, QDIPs promise to be more advantageous for photon detection because of the three-dimensional carrier confinement in the active region, quantum dots. These advantages include being sensitive to normal incidence light, higher optical gain, longer photo-excited carrier lifetime, and lower dark current[15, 16]. However, current QDIPs using quantum dots by self-assembled growth method can still not achieve the performance as expected, mostly because of the non-uniformity of quantum dot sizes[17].

Here we will present an alternative method of forming QDIPs to detect electromagnetic radiation in terahertz region using electrical confinement method. We have previously shown that lateral electric field applying on quantum wells combining with quantum barriers confinement will induce a three-dimensional confinement for carriers and form a quantum dot[18]. Here we apply the idea of forming a quantum dot into making a QDIP device to detect terahertz radiation and model the performance characteristics of the device, such as absorption spectra, noise current, responsivity, and detectivity. We demonstrate that the energy state levels in the quantum dots and absorption spectra can be tuned by the voltage being applied. The effective quantum dot sizes by the method can be quite uniform because of the well defined electrical confinement. Finally, we discuss possible improvement for the photodetector.

2. Detector device structure

A schematic 3D view of the proposed photodetector structure is shown in Fig. 1(a), and Fig. 1(b) is the cross-section and top side view of the device structure. The injector contact is on the top of the device, and the gate contact surrounding the injector induces the lateral electrical confinement on the quantum wells below. Between the gate and top contacts, there is a layer of electrical insulator. The diameter of the injector contacts is designed to be 200 nm. Each effective quantum dot has an injector, and all the gate contacts for the dots are connected to each other with the same voltage. The semiconductor structure used for simulations includes a surrounding gate contact on the top (30 nm thickness of $In_{0.53}Ga_{0.47}As$ with an acceptor doping density of $5x10^{17}$ cm^{-3}), a top contact layer (50 nm thickness of $In_{0.53}Ga_{0.47}As$ with a donor doping density of $5x10^{16}$ cm^{-3}), quantum well active layers consisting of $In_{0.53}Ga_{0.47}As$ and $In_{0.52}Al_{0.48}As$ (thickness of 300 nm with an average donor doping density of $3.5x10^{16}$ cm^{-3}), and a bottom layer of doped $In_{0.53}Ga_{0.47}As$ as ground contact.

When a negative voltage is applied on the gate contact, electrons are depleted and confined in the central region below the injector, while they are also longitudinally confined in the quantum wells by quantum barriers. The strong electrical confinement on the quantum wells breaks the in-plane periodic potential of the wells and splits continuous energy bands into discrete energy states or levels. Changing the gate voltage it can induce different confinements and change the energy levels in the dots. The inter-level separations can also be tuned and hence different wavelength detection for the photodetectors can be achieved by changing the gate voltage.
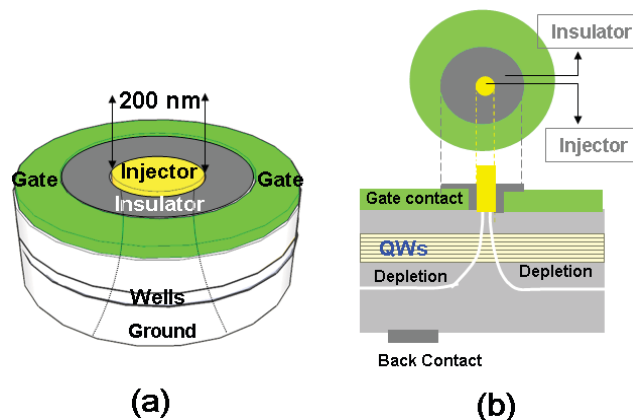

Figure 1- (a) 3D view of the proposed QDIP device structure, and (b) cross-section and top view of the QDIP device

3. Modeling theory

We used drift-diffusion equations including Poisson and continuity equations[19] to simulate the electrostatic potential distributions and carrier depletion effect in the device. Using the result of electrostatic potential distributions, we solved three-dimensional Schrödinger equation to calculate the electron energy levels and states in the QD. All the simulations are performed by our custom numerical finite element method (FEM) method.

The Poisson and continuity equations can be expressed as

$$\nabla \cdot (\varepsilon_0 \varepsilon_i \nabla \phi) = -q(p - n + N^+) \tag{1}$$

$$\nabla \cdot (\mu_n \nabla E_{Fn}) = qR \tag{2}$$

$$\nabla \cdot (\mu_p \nabla E_{Fp}) = -qR \tag{3}$$

$$R = \frac{n_i^2 \exp(\dfrac{E_{Fp} - E_{Fn}}{kT})}{\tau_n(p + n_i) + \tau_p(n + n_i)} \tag{4}$$

where ε_i is the relative permittivity for different semiconductor layers, ϕ is the electrostatic potential, n and p are concentration distributions for electrons and holes respectively, N^+ is the ionized doping density distribution, q is the electron charge, μ_n and μ_p are the mobility for electrons and holes, E_{Fn} and E_{Fp} are the quasi-Fermi levels for electrons and holes respectively, R is the net recombination-generation rate, n_i is the neutral electron concentration, T is the temperature, and τ_n and τ_p are the lifetime of electrons and holes respectively. The quasi-Fermi levels are used in the model to include both electric field drift and carrier diffusion processes. All the variables in the equations are three-dimensional. However, since the device structure has a cylindrical symmetry, we simplified the equations to two-dimensional ones with added components in the equations, and it will not affect the accuracy of the results. To simplify the equations, supposing a variable $\vec{f} = f_r \vec{r} + f_z \vec{z}$ the divergence of the variable with cylindrical symmetry can be given by

$$\nabla(f) = (\frac{\partial}{\partial r} + \frac{1}{r}) f_r + \frac{\partial f_z}{\partial z} \tag{5}$$

$$\nabla \cdot (k\nabla f) = \frac{\partial}{\partial r}(k\frac{\partial f}{\partial r}) + \frac{k}{r}\frac{\partial f}{\partial r} + \frac{\partial}{\partial z}(k\frac{\partial f}{\partial z}) = \nabla^* \cdot (k\nabla^* f) + \begin{Bmatrix} \dfrac{k}{r} \\ 0 \end{Bmatrix} \nabla^* f \tag{6}$$

where k is some constant in the formula, ∇^* is the Cartesian Nabla operator in two-dimensional system.

The Schrödinger equation in the cylindrical coordinates can be written as

$$-\frac{\hbar^2}{2m^*}[\frac{1}{r}\frac{\partial}{\partial r}(r\frac{\partial}{\partial r}) + \frac{1}{r^2}\frac{\partial^2}{\partial \theta^2} + \frac{\partial^2}{\partial z^2}]\psi(r,\theta,z) + V(r,z)\psi(r,\theta,z) = E\psi(r,\theta,z) \tag{7}$$

when $\hbar$ is the plank's constant, m^* is the effective mass for electrons at different semiconductor layers, ψ is the electron state wavefunction, $V(r, z)$ is the potentials obtained from above, and E is the electron energy level. The solution for the wave function can be written as

$$\psi(r,\theta,z) = (\frac{1}{\sqrt{2\pi}})e^{im\theta}R_m(r)\varphi_l(z) \tag{8}$$

where $R_m(r)$ is the Bessel function of the radius r, and $\varphi_l(z)$ is a slowly varying function of r.

To accurately model the device and obtain the solutions, we considered and added several nonlinear effects in our solver, such as incomplete ionization of dopants and carrier mobility saturation effect. Besides, we also considered the effects of the electron effective mass as a function of the energy levels[20] when solving the Schrödinger equation, so we kept updating the effective mass with the energy level solution until the solution was almost unchanged.

For the absorption spectral calculations for the quantum dots, we used the formula shown in ref. 21, but we also added the in-plane fill factor η of quantum dots since only the area with quantum dots can effectively absorb the light.

$$\alpha(\hbar\omega) = \eta(\frac{\omega}{n_r c \varepsilon_0})\frac{2}{V}\sum_{i,j}\frac{\left|e \cdot \hat{u}_{i,j}\right|^2 (\Gamma/2)}{(E_j - E_i - \hbar\omega)^2 + (\Gamma/2)^2}(f_j - f_i) \tag{9}$$

where n_r is the average refractive index of the active region, V is the QD volume (the factor of 2 is considering the electrons spin degeneracy), $\hat{u}_{i,j}$ is the transverse optical dipole moment values (which can be calculated by wavefunctions intergral), Γ is the full width at half maximum (FWHM) of the absorption broadening (here is mainly caused by inhomogeneous broadening), and f is the Fermi-Dirac distribution function. Since we are mostly considering the broadening due to inhomogeneous broadening under quasi-parabolic potentials, Γ can be written as $\Gamma = 4E_n\xi$ [22], where ξ is the size deviation and E_n is the nth eigenstate energy level. Here we used a size deviation of 1% corresponding to a deviation of 2 nm for 200 nm diameter of nanoholes, which is achievable using our developed Super Lens Lithograph [23-25], a fast and economic method to generate highly dense and uniform nanohole arrays over large areas.

4. Simulation results & analysis

Solving Poisson and continuity equations, we have calculated the electrons concentration in the quantum dot device structure and simulated the confinement effects for different gate voltages. Fig. 2(a) shows the electron concentration distribution with an injection voltage V_a =0 V and gate voltage V_g = -5 V. It clearly shows most electrons are depleted and confined into a nano-channel below the injector. The color bar shows the relative electron concentration distributions. Figure 2(b) shows the confinement effect with an increased gate voltage of V_g = -2 V. The confinement effect is becoming weaker due to the weaker depletion of the gate voltage. The depletion width is smaller and central confinement region below the injector is wider. This confirms the tunability of the proposed device by the gate voltage. Fig. 3(a) is the electrostatic potential distribution under a gate voltage of V_g = -5 V with potential contour curves in the plot and Fig. 3(b) shows the effective radial potentials in the center of quantum wells region as a function of the radial distance from the injector center with different gate voltages. The parabolic potentials can effectively trap electrons to the central regions similar as the quantum barriers confine the electrons in the quantum wells. In fact, only the change of the potential energy is effective for the confinement, while the values of them are not important.
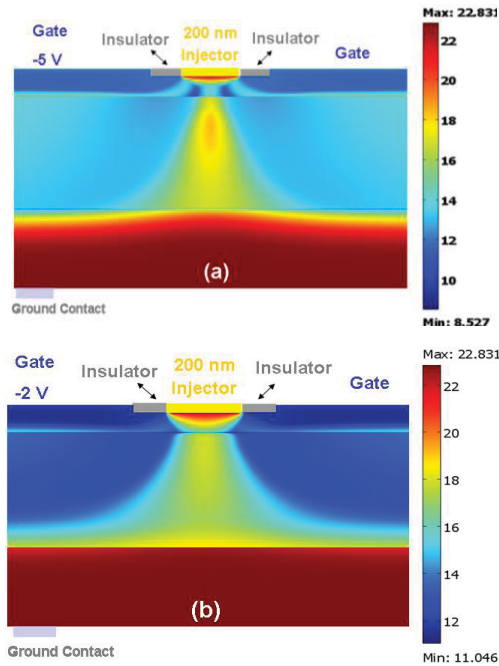
Figure 2- (a) Electrons concentration distribution in the device under a gate voltage $V_g = -5$ V, and (b) the concentration distribution under a different gate voltage $V_g = -2$ V, which shows a weaker confinement for electrons.
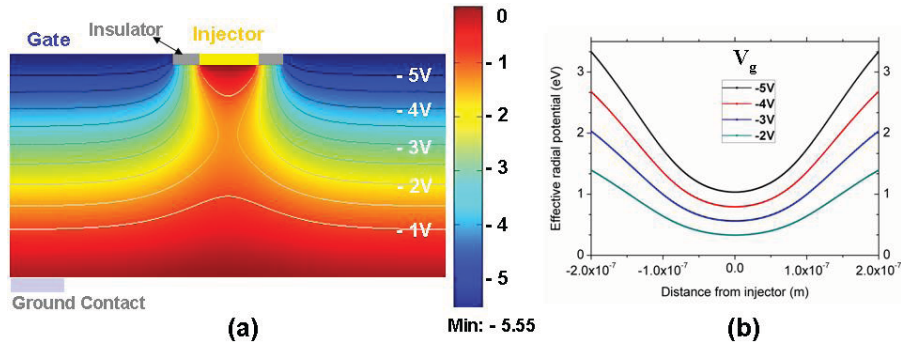

Figure 3- (a) Electrostatic potential distribution in the device under $V_g = -5$ V, and (b) the effective radial potentials in the center of quantum wells as a function of the radial distance from the injector with different gate voltages.

Fig. 4(a) shows the first four wavefunction states *s, p, d,* and *f,* formed by the parabolic wells as a function of the gate voltages. With a more negative voltage, the energy states blue shift. Fig. 4(b) shows the energy separations between the adjacent energy levels at different gate voltages. There are many electron states formed in the quantum well layers because of the weak lateral electrical confinement. The main effects caused by the electrical confinement are: (1) a pronounced blue-shift of the energy levels in the dot, (2) the tunable energy level separation, and (3) the reduction of homogeneously broadened absorption.
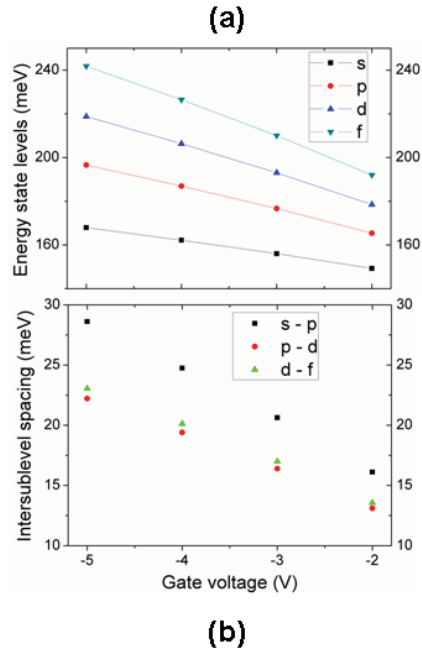
(a)

(b)

Figure 4- (a) The positions of *s, p, d,* and *f* electron states as a function of the gate voltages, and **(b)** the energy level separation between the adjacent states, which is voltage controllable.

Figure 5(a) shows the absorption spectral coefficients due to the transverse transitions of electrons at different gate voltages with an injection voltage of V_a= 0 V. The peak absorption wavelength can be tuned from ~50 to ~85 µm with the gate voltages from -5 to -2 V. The temperature T and Γ decide the sharpness of the absorption curve, and the carrier concentration and density of dots decide the intensity of the absorption. Fig. 5(b) shows the absorption spectra under different gate voltages with the injection voltage of V_a= 5 V at 77 K. Because of the applied injection voltage, the parabolic well in the quantum well region becomes steeper, and the detection region blue-shift. The peak detection wavelength at -5 V of the gate voltage can reach an even higher frequency.
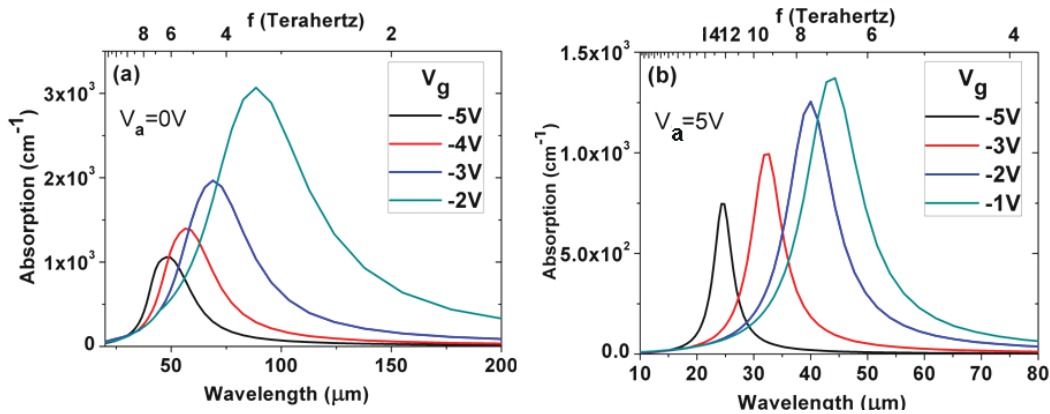

Figure 5- Normal-incidence absorption spectra coefficient at 77 K for the quantum dots, (a) peak detection cover from ~50 to ~85 µm under the injection voltage V_a=0V, **(b)** the detection blue shift with V_a=5V.

Using the Fowler-Nordheim tunneling and thermionic escape model, we calculated the dark current density and noise current of the photodetector at 77 K for different gate voltages. The dark current J_d mainly consists of the tunneling escape current J_t and the band escape thermionic current J_b [26]. The tunneling escape current density J_t is

$$J_t = q\frac{m^*}{\pi\hbar^2}N\frac{d_b}{L}\frac{\mu F\tau}{L[1+(\frac{\mu F}{v_{sat}})^2]^{1/2}}*$$

$$\int_0^{Ec-E0}(\frac{1}{1+\exp(\beta(E+E_1-E_f))})(\frac{E_1+\gamma E}{h})\exp[-\frac{4}{3}(\frac{2m_b^*}{\hbar})^{1/2}\frac{(E_c-(E_1+\gamma E))^{3/2}}{qF}]dE$$

(10)

and the band escape thermionic current J_b is

$$J_b = qN\frac{1}{2\pi^2}(\frac{2m^*}{\hbar^2})^{3/2}\frac{\mu F}{[1+(\frac{\mu F}{v_{sat}})^2]^{1/2}}\int_{Ec}^{\infty}(\frac{1}{\exp(\beta(E-E_f)+1)})\sqrt{E}\,dE$$

(11)

where m^* is the well effective mass, N is the number of quantum wells ~12, d_b is the barrier length, L is the active region length, μ is the electron mobility on the barrier layers, F is the electric field, τ is the carrier lifetime, v_{sat} is the electron's saturation velocity, E_1 is the ground energy level, γE is the effective planar energy for tunneling through the barrier, and m_b is the barrier effective mass. Fig. 6(a) shows the calculation result of the dark current density as a function of electric field and the bias voltage at different gate voltages. A more negative gate voltage leads to a higher dark current density, because the energy levels are closer to barrier and carriers are easier to escape. The noise current I_n can be expressed as $I_n = \sqrt{4qg\Delta f I_d}$, where g is the gain of detector defined as $\frac{\tau}{\tau_{transit}}$, Δf is the bandwidth, I_d is the dark current, and $\tau_{transit}$ is the transit time through the barriers for carriers. Fig. 6(b) shows the current noise in the device with different gate voltages.
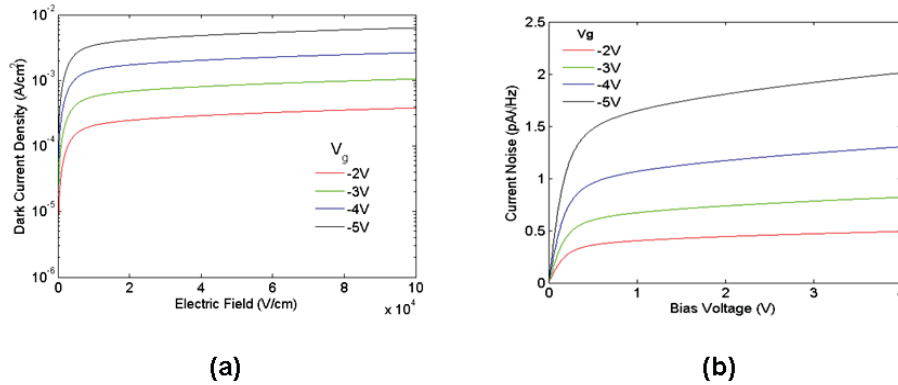

(a)   (b)

Figure 6- (a) The dark current density in the QDIP device, and (b) the current noise under different gate voltages

The responsivity and detectivity of a photodetector are

$$R_p = \frac{q}{\hbar\omega}g\eta = \frac{q}{\hbar\omega}g[1-\exp(-\alpha L)]\frac{\tau_r}{\tau_r+\tau_e}$$

(12)

$$D^* = R_p\sqrt{A\Delta f}\Big/I_n$$

(13)

where $\hbar\omega$ is the peak photon energy (obtained from the absorption spectral plots), τ_r is the carrier recombination time, τ_e is the escape time, and $\dfrac{\tau_r}{\tau_r + \tau_e}$ is the escape probability, which can be fit as a function of the bias voltage[27]. The peak responsivity of our detector at different gate voltages is shown in Fig. 7(a), and the calculated results of the detectivity with different gate voltages are shown in Fig. 7(b). With an increased bias voltage, the detectivity quickly goes up and then drops back to an almost constant. The peak detectivity is almost as large as 1.7×10^9 cmHz$^{1/2}$/W at V_g of -2 V, which is contributed by the highly uniform effective quantum dot sizes.
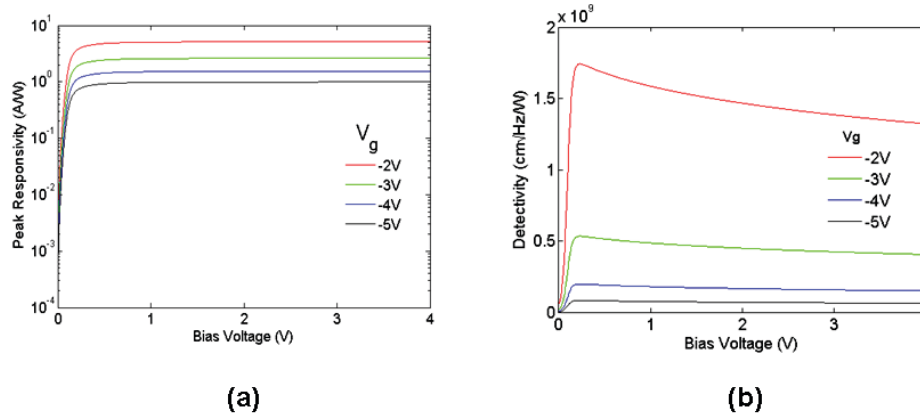

Figure 7- (a) Peak responsivity for the photodetector, and (b) detectivity at different gate voltages from -2 to -5 V

To improve the performance of the proposed terahertz photodetector, we can increase the absorption coefficients of quantum dots by increasing quantum dot density. To increase the density the processing technique of fabricating uniform nanohole arrays needs to be further improved. Currently the period of the array we used is 500 nm, so there should still be enough room for further reducing the period. In addition, more optimized quantum well structures needs to be designed. Because most energy levels are below the quantum barrier for the current structure, although the dark current can be very low, the escape probability for photo-excited carriers can also be low. Thirdly, since terahertz photodetectors are always working at very long wavelength, the electron-phonon scattering would reduce the lifetime of photo-excited carriers heavily, and hence a lower temperature operation could greatly enhance the gain and detectivity. Finally, novel device structure can also be designed and optimized to increase the confinement effects of the gate contact, such as keeping the quantum well active layers close to the surface of the gate contact.

5. Conclusions

We have presented an electrical method to form quantum dot infrared photodetector for the electromagnetic wave detection in terahertz region. We simulated the electrical confinement and the energy levels in the quantum dots. We also demonstrated the normal-incidence absorption spectra under different gate voltages. The absorption of the detector can cover the terahertz region from ~3.3 up to ~12.5 THz with a peak absorption in the range of 10^3 cm^{-1} by controlling the gate voltage. The performance characteristics of current noise, peak responsivity, and detectivity of the photodetector were also calculated and demonstrated. With improved processing of forming a denser quantum dot array and a further optimal design of band and device structure, the photodetector can be further improved in performance for terahertz detection.

References

[1] R. Kohler, A. Tredicucci, F. Beltram, H. E. Beere, E. H. Linfield, A. G. Davies, D. A. Richie, R. C. Iotti, and F. Rossi, "Terahertz semiconductor-heterostructure laser," Nature 417, 156-159 (2002)

[2] B.B. Hu and M.C. Nuss, "Imaging with terahertz waves," Opt. Lett 20, 1716-1719(1995)

[3] P. Y. Han, G. C. Cho, and X. C. Zhang, "Time-domain transillumination of biological tissues with terahertz pulses," Opt. Lett. 25, 242-244 (2000)

[4] D. M. Mittleman, R. H. Jacobsen, and M. C. Nuss, "T-ray imaging," IEEE J. Sel. Top. Quant. Electron. 2, 679 (1996)

[5] P.H. Siegel, "THz Instruments for Space," IEEE Trans. on Antennas and Propagation 55, 2957-65 (2007)

[6] T.R. Globus, D.L. Woolard, T. Khromova, T.W. Crowe, M. Bykhovskaia, B.L. Gelmont, J. Hesler and A.C. Samuels, "Thz-. Spectroscopy of Biological Molecules," J. of Biological Physics 29, 89-100 (2004)

[7] B. S. Williams, S. Kumar, H. Callebaut, Q. Hu, and J. S. Reno, "Terahertz quantum-cascade laser operating up to 137 K," Appl. Phys. Lett. 83, 5142-5144 (2003)

[8] A. L. Betz, R. T. Boreiko, B. S. Williams, S. Kumar, Q. Hu, and J. L. Reno, "Frequency and phase-lock control of a 3 THz quantum cascade laser," Opt. Lett. 30, 1837-1839 (2005)

[9] A. Tredicucci, R. Köhler, L. Mahler, H. E. Beere, E. H. Linfield, and D. A. Ritchie, "Terahertz quantum cascade lasers—first demonstration and novel concepts," Semicond. Sci. Technol. 20, S222–S227 (2005)

[10] D. T. Hodges and M. McColl, "Extension of the Schottky barrier detector to 70 µm (4.3 THz) using submicron-dimensional contacts," Appl. Phys. Lett. 30, 5-7 (1977)

[11] Y. Cai, I. Brener, J. Lopata, J. Wynn, L. Pfeiffer, and J. Federici, "Design and performance of singular electric field terahertz photoconducting antennas," Appl. Phys. Lett. 71, 2076-2078 (2007)

[12] J. P. Rice, E. N. Grossman, and D. A. Rudman, "Antenna-Coupled High-Tc Air-Bridge Microbolometer on Silicon," Appl. Phys. Lett. 65, 773 (1994)

[13] H. C. Liu, C. Y. Song, A. J. SpringThorpe, and J. C. Cao, "Terahertz quantum-well photodetector," Appl. Phys. Lett. 84, 4068 – 4070 (2004)

[14] X. H. Su, J. Yang, P. Bhattacharya, G. Ariyawansa, and A. G. U. Perera, "Terahertz detection with tunneling quantum dot intersublevel photodetector," Appl. Phys. Lett. 89, 031117-9 (2006)

[15] J. C. Campbell and A. Madhukar, "Quantum dot infrared photodetector," Proc. IEEE 95, 1815-1827 (2007)

[16] S. Krishna, S. Raghavan, G. von Winckel, A. Stintz, G. Ariyawansa, S. G. Matsik, and A. G. U. Perera, "Three-color InAs/InGaAs quantum-dots-in-a-well detector," Appl. Phys. Lett. 83, 2745-7 (2003)

[17] J. Phillips, "Evaluation of the fundamental properties of quantum dot infrared detectors," J. Appl. Phys. 91, 4590-4594 (2002)

[18] W. Wu, D. Dey, O. G. Memis, and H. Mohseni, "Modeling and fabrication of electrically tunable quantum dot intersubband devices," Appl. Phys. Lett. 94, 193113-5 (2009)

[19] S. L. Chuang, "Physics of Optoelectronic Devices", Wiley, New York, 24-28 (1995)

[20] N. Kotera, and K. Tanaka, "Determination of electron effective mass from optical transition energy in InGaAs/InAlAs quantum wells," Physica E 32, 199-202 (2006)

[21] E. H. Hoffman, and S. L. Chuang, "Theory for Intersubband Absorption in Quantum Dots," Proc. SPIE 5349, 90-94 (2004)

[22] W. Y. Wu, J. N. Schulman, T. Y. Hsu, and U. Efron, "Effect of size nonuniformity on the absorption spectrum of a semiconductor quantum dot system," Appl. Phys. Lett. 51, 710-712 (1987)

[23] W. Wu, A. Katsnelson, O. G. Memis, and H. Mohseni, "A deep sub-wavelength process for the formation of highly uniform arrays of nanoholes and nanopillars," Nanotechnology 18, 485302 (2007)

[24] W. Wu, D. Dey, O. G. Memis, A. Katsnelson, and H. Mohseni, "Fabrication of Large Area Periodic Nanostructures Using Nanosphere Photolithography," Nanoscale Res Lett. 3, 351 (2008)

[25] W. Wu, D. Dey, A. Katsnelson, O. G. Memis, and H. Mohseni, "Large areas of periodic nano-holes perforated in multi-stacked films produced by lift-off," J. Vac. Sci. Technol. B, 26, 1745-1747 (2008)

[26] A. Gin, B. Movaghar, M. Razeghi, and G. J. Brown, "Infrared detection from GaInAs/InP nanopillar arrays," Nanotechnology 16, 1814-1820 (2005)

[27] H. Lim, B. Movaghar, S. Tsao, M. Taguchi, W. Zhang, A. A. Quivy, and M. Razeghi, "Gain and recombination dynamics of quantum-dot infrared photodetectors," Phys. Rev. B 74, 205321 (2006)